Defect-concentration-mediated T-Nb_2O_5 anodes for durable and fast-charging Li-ion batteries

Yongjian Zheng, Zhenguo Yao, Zulipiya Shadike, Meng Lei, Jianjun Liu, and Chilin Li *

Y. Zheng, M. Lei, Prof. C. Li

CAS Key Laboratory of Materials for Energy Conversion, Shanghai Institute of Ceramics, Chinese Academy of Sciences, Shanghai 201899, China. Email: chilinli@mail.sic.ac.cn

Y. Zheng, Dr. Z. Yao, Prof. J. Liu, Prof. C. Li

Center of Materials Science and Optoelectronics Engineering, University of Chinese Academy of Sciences, Beijing 100049, China.

Prof. Z. Shadike

Institute of Fuel Cells, Interdisciplinary Research Center, School of Mechanical Engineering, Shanghai Jiao Tong University, Shanghai 200240, China.

Y. Zheng, Dr. Z. Yao, M. Lei, Prof. J. Liu, Prof. C. Li

State Key Laboratory of High Performance Ceramics and Superfine Microstructure, Shanghai Institute of Ceramics, Chinese Academy of Sciences, 585 He Shuo Road, Shanghai 201899, China.

Dr. Z. Yao

BTR New Material Group CO., LTD., GuangMing New District, Shenzhen 518106, China.

This is the author manuscript accepted for publication and has undergone full peer review but has not been through the copyediting, typesetting, pagination and proofreading process, which may lead to differences between this version and the Version of Record. Please cite this article as doi: 10.1002/adfm.202107060.

Abstract: Metastable orthorhombic niobium pentoxide (T-Nb_2O_5) is a promising anode material to fulfill the requirements for high-rate Li-ion batteries (LIBs). Stoichiometric T-Nb_2O_5 is plagued by low electric conductivity and particle pulverization after repeated charge/discharge process. In this work, oxygen vacancies are implanted into T-Nb_2O_5 particles via acid immersion of $Nb_2O_5 \cdot nH_2O$ with the formation of Lewis acid sites. The multiple characterizations and simulations reveal the lengthening of Nb-O bonds and the transformation from NbO_7 pentagonal bipyramids and NbO_6 tetragonal bipyramids in T-Nb_2O_{5-x}. The enrichment of oxygen vacancies endows T-Nb_2O_{5-x} with much higher electric conductivity, better electrochemical kinetics, larger pseudocapacitive contribution. O-doped g-C_3N_4 is creatively proposed as trace oxygen pump to repair excessive oxygen vacancies, and it also serves as sacrifice template for Nb_2O_{5-x} growth to construct porous and monolithic electrode network. Defect-modulated Nb_2O_{5-x} displays extraordinary cycling stability (164 mAh/g at 5 C after 1100 cycles), high capacity retention (104 mAh/g) at ultrahigh rate (25 C) and large areal capacity (0.74 mAh/cm^2) under high mass loading (4 mg/cm^2). The practical prospect is proved by Nb_2O_{5-x}/$LiNi_{0.8}Co_{0.1}Mn_{0.1}O_2$ full cells with high average platform (2.12 V) and high specific capacity (229 mAh/g). The oxygen-defect modulation strategy on oxide anodes provides alternative solution to fast-charging and durable LIBs.

Keywords: oxygen vacancies, T-Nb_2O_5, intercalation pseudocapacitance, lithium ion battery, fast charging

INTRODUCTION

With the commercialization and universalization of Li ion batteries (LIBs), especially for the development of electrical vehicles, more parameters of batteries are required to grasp the customers' attention except for the conventional concerns on safety and energy density, like durability and charging rate.[1] To further decrease the charging time (80% charged within 10-15 minutes), tremendous efforts have been devoted to the exploration of quickly chargeable and highly reversible anode materials.[2] $Li_4Ti_5O_{12}$, widely accepted as a promising anode candidate for commercial LIBs, displays the evidently descending capacity with the increase of current density. Its excellent electrochemical performance overly relies on nano-structured design and composition with conductive wires.[3] In comparison, Nb_2O_5 is also an appealing insertion-type anode material, but with much higher electric conductivity (3.4×10^{-6} S/cm vs. 10^{-8}-10^{-13} S/cm for $Li_4Ti_5O_{12}$, at 300 K) and relatively higher theoretical capacity (200 mAh/g vs. 175 mAh/g for $Li_4Ti_5O_{12}$).[4,5] Four different phases of Nb_2O_5 can be obtained (e.g. by the oxidization of NbO_2 at stepwise increasing temperature), including pseudohexagonal Nb_2O_5 (denoted as TT-Nb_2O_5), orthorhombic Nb_2O_5 (denoted as T-Nb_2O_5), bladed Nb_2O_5 (denoted as B-Nb_2O_5) and monoclinic Nb_2O_5 (denoted as H-Nb_2O_5).[6] H-Nb_2O_5 is the most stable phase at room temperature, and it delivers the highest initial capacity but decays rapidly, while T-Nb_2O_5 enables the excellent rate and cycling performance.[7] TT-Nb_2O_5 has the similar structure as T-Nb_2O_5, however delivers the inferior electrochemical performance than T-Nb_2O_5. Recently Grey and coworkers found that micrometer-scaled T-Nb_2O_5 without intentional nanostructuring, can achieve the desirable high-rate performance, which is ascribed to the self-supporting layered "room and pillar" structure and the resultant two dimensional (2D) Li-ion migration channel.[6] A thick T-Nb_2O_5 electrode (40 μm in thickness) shows a markedly better rate capability than $Li_4Ti_5O_{12}$ above 30 C and its capacity is preserved at ~40 mAh/g at ultrahigh 1000 C rate, which is attributed to a capacitive storage mechanism termed as intercalation pseudocapacitance as reported by Dunn et al.[8] T-Nb_2O_5, as a promising alternative anode, remains to be further explored to compete with commercially available anode materials.

As known, stoichiometric Nb_2O_5 is classified into electrical insulator with a band gap of 4 eV. T-Nb_2O_5 anode is plagued by its low electronic conductivity, which likely results in capacity decaying during iterative charge/discharge processes.[9] Constructing the delicate nanostructure (e.g. nanosheet, nanowire and mesoporous particle) is the most universal method, and it is beneficial to the immersion of electrolyte and shortening of ion diffusion distance. On the other hand, the integration with carbonaceous matrix (or wiring) is an efficient method to promote the electrical conductivity of electrode network. Duan et al. combined Nb_2O_5 with three-dimensional (3D) graphene network, achieving an ultrahigh mass loading (~10 mg/cm^2) but not at the expense of capacity shrinkage.[10] Carbon coating decorated T-Nb_2O_5 possessed a highly reversible capacity of 169.6 mAh/g at 2 A/g after 2000 cycles as reported by Mai et al.[11] However most of the conductive assistant components are electrochemically inactive and would cause the decrease of practical specific capacity of electrode. More exposure of nanostructured active material to electrolyte would aggravate the formation of solid electrolyte interphase (SEI) and electrolyte consumption. To avoid the dilemma, heteroatom decoration and bulk particle architecture contribute to mitigate the above-mentioned problems. Superficial functional layer doped with trace amount of silver and nitrogen imparts Nb_2O_5 particles with good electrical conductivity and excellent electrochemical performance, as reported by Kim et al.[12] What's more, a small amount of KF was introduced into T-Nb_2O_5 to fabricate a bulk H-Nb_2O_5 with in-situ wiring of conductive tetragonal tungsten bronze (TTB) framework in our previous work.[13,14] Recently, the solid-solution compounds with Wadsley-Roth crystallographic shear phases, like WO_3-Nb_2O_5, TiO_2-Nb_2O_5 and CuO-Nb_2O_5, have attracted much attention, and they enable the rapid and trustworthy Li diffusion inside the particles even at micrometer scale and the intercalation of abundant Li at ultrahigh rate.[15-17] The incorporation of oxygen vacancies is an alternative method for the microstructure modulation.

Oxygen vacancy engineering in transition metal oxides (TMOs), referring to the amount and distribution of oxygen vacancies, emerged as a valid and universal method to optimize their energy storage and conversion performance. Oxygen vacancies tend to induce the concomitant appearance of free electron and multivalence of transition metal in a compound,

such as TiO_{2-x}, MoO_{3-x} and MnO_{2-x}.[18-20] Plenty of works indicated the enhancement of electric conductivity in O-deficient TMOs, which grants the better electrode reaction kinetics. In the oxygen deficient $LiNi_{0.5}Mn_{1.5}O_{4-x}$, the preferable formation of vacancies near Ni-rich domains enables the redistribution of local charge state and stabilization of lattice Li ions.[21] In addition, the absence of oxygen in lattices was reported to enlarge the interlayer spacing and mitigate the steric hindrance of ion insertion at the premise of keeping the desired crystal structure.[19,22] Oxygen vacancies in MoO_{3-x} were also found to facilitate the pseudocapacitive charge storage.[19] Recently, oxygen vacancies were proved to benefit the pseudocapacitive contribution in T-Nb_2O_5, while there is no poignant analysis between oxygen vacancies and crystal structure.[23] More works are required to clarify the correlated lattice sites and specific roles of oxygen vacancies in T-Nb_2O_5 framework. Note that the thermal reduction environment is often used to synthesize the defective TMOs, however it is prone to cause the excess escape of lattice O and lead to the heavily defective structure with the degradation of electrochemical stability and shrinkage of reversible capacity.[24,25] Therefore it is highly desired to explore the solution to the accurate manipulation of O defects with moderate concentration.

Herein, we innovatively implant oxygen vacancies into T-Nb_2O_5 through acid treatment at room temperature and use O-doped graphitic C_3N_4 (O-g-C_3N_4) as oxygen origin to repair redundant oxygen vacancies. O-g-C_3N_4 is proposed as a trace oxygen supplier for the first time, enabling the successful decrease of O vacancy concentration from 19 μmol/g for Lewis acid Nb_2O_5 (denoted as L-NbO) to 0.31 μmol/g for O-g-C_3N_4 templated Nb_2O_5 (denoted as CN-NbO), without the serious compromise of electrical conductivity (from 6.8×10^{-5} S/cm for L-NbO to 2.7×10^{-5} S/cm for CN-NbO at 300 K), which is still two magnitude higher than that of commercial stoichiometric T-Nb_2O_5. We find that superfluous vacancies are not conductive to the structural stability of T-Nb_2O_5 as anode and affect its cycling durability. The defect-mitigated CN-NbO displays the higher capacities of 183 and 104 mAh/g at 5C and 25C respectively, compared with the defect-rich L-NbO. CN-NbO also enables the better cycling stability for at least 1100 cycles even at 5C. However the heavily defect-doped L-NbO exhibits a more endurable rate performance and higher pseudocapacitive contribution

in view of its higher intrinsic conductivity, which allows the increase of areal loading of active grains up to 4 mg/cm^2.

RESULTS AND DISCUSSION

The oxygen-defected Nb_2O_5 was fabricated through acid immersion and conventional sintering with the bottom-up method illustrated in Figure 1. Hydrated Nb_2O_5 ($Nb_2O_5 \cdot nH_2O$) was obtained through the direct hydrolysis of niobium ethoxide ($Nb(OEt)_5$) with deionized water poured . Inside the amorphous structure of $Nb_2O_5 \cdot nH_2O$, H_2O molecules bridge Nb-O polyhedrons through hydrogen bonds between oxygen atoms and hydrogen atoms to maintain the disordered structure in $Nb_2O_5 \cdot nH_2O$.[26] After immersion in HCl solution, more protons are prone to be absorbed onto the Brønsted acid (BA) sites, namely the vertex of Nb-O polyhedrons.[27] With the removal of BA sites in the form of water (i.e. a terminal hydroxyl group and a proton) during the annealing process, oxygen vacancies are naturally created at the positions where two BA sites are adjacent, leading to the generation of Lewis acid sites inside O-vacancy-rich L-NbO.[27] To suppress the excess formation of oxygen vacancies, O-g-C_3N_4 was introduced into the synthesis of CN-NbO. O-g-C_3N_4 is expected to provide the active sites for the adsorption of Nb^{5+} and H^+ in $Nb(OEt)_5$/ethanol solution as the mechanism of graphene oxide.[28] This adsorption behavior can compete with the H^+ absorption on Nb-O BA sites via hydrogen bonding, and alleviate the formation of O vacancies during annealing. On the other hand, the doped O resource in O-g-C_3N_4 can detach from the precursor template when annealed in insert atmosphere and offers oxygen atoms to fill up the defect sites and repair the crystal structure of T-Nb_2O_5. According to the reported thermogravimetric analysis of g-C_3N_4,[29] O-g-C_3N_4 completely volatilizes into gas at 750 ^oC (i.e. our annealing temperature). It is beneficial for the release and migration of oxygen atoms, which are smartly supplemented to the defect sites of L-NbO.

The X-ray diffraction (XRD) patterns in Figure 2a show that CN-NbO, L-NbO and C-NbO (i.e. annealed commercial T-Nb_2O_5) belong to orthorhombic phase (T-Nb_2O_5, JCPDS No.30-0873). Three strongest peaks below 40 degree are indexed to (001), (180) and (181) respectively. According to Bragg diffraction formula, there is no obvious change on lattice parameters deduced from the peaks at the same positions with the change of lattice O concentration. The Rietveld refinement of L-NbO indicates the consistent cell parameters (a = 6.204 Å, b = 29.142 Å, c = 3.939 Å) and volume (V = 710.247 $Å^3$) with the corresponding theoretical parameters of T-Nb_2O_5,[11] as showed in Figure S1 and Table S1. Comparing the width at half maximum of these diffraction peaks, the value for (001) peak is smallest for all three samples and its intensity is also higher for L-NbO and CN-NbO, indicating that the formation of O vacancies is favorable for the growth of crystal grains along the [001] direction. Note that, for L-NbO, the dominant (180) and (181) peaks appear to merge with the nearby peaks indexed to (200) and (201) respectively, and it should be ascribed to the nano-structuring of L-NbO particles with diffraction peak broadening. The existence of excess defect sites in L-NbO is also responsible for the disordering of crystalline domains and broadening of XRD peaks. With the attenuation of O defects in CN-NbO, the peak splitting phenomenon recovers to the situation appearing in C-NbO. In the layered structure of T-Nb_2O_5 crystal, NbO_6 octahedra and NbO_7 pentagonal bipyramids interconnect with each other by either edge-sharing or corner-sharing manner on (001) planes in Figure 2b.[6] These alternating layers connect with each other along the [001] direction through Nb-O-Nb bonds, leaving the stable two-dimensional (2D) channels allowing favorable Li migration (Figure 2c). NbO_6 octahedra are highly distorted in T-Nb_2O_5 due to the second-order Jahn-Teller effect and electrostatic repulsion, and Nb sites partially occupied by Nb(Ⅳ) can relax lattice stress but without the destroying of Li^+ diffusion paths.[30] With limited lattice spacing and rigid crystal structure, the introduced oxygen defects can trigger the formation of desired Nb(Ⅳ) sites with relaxation of Jahn-Teller distortion. The colors of C-NbO, L-NbO and CN-NbO are distinct from each other as shown in Figure 2d. The white commercial T-Nb_2O_5 powder becomes blue after annealing in N_2. After the import of oxygen vacancies, L-NbO displays dark gray close to the color of carbon black (CB). While with the participation of

O-g-C_3N_4, the powder of CN-NbO appears gray, but with an obviously different gray level compared with L-NbO. Different coloring indicates the different state of electrons on *d* orbits, as the activation and hopping of electrons play a pivotal role in the light absorption and charge transportation. Electric conductivity is obtained through a four-probe method, and it is estimated to be 6.8×10^{-5} and 2.7×10^{-5} S/cm for defect-rich L-NbO and defect-mitigated CN-NbO respectively, both much higher than that of C-NbO (1.3×10^{-7} S/cm). Note that the post-healing of O vacancies does not compromise the electric conductivity, indicating that a trace amount of defects is sufficient to activate the conductivity performance.

Scanning electron microscopy (SEM) and transmission electron microscopy (TEM) images show the morphology and size distribution of CN-NbO, L-NbO and C-NbO powders. The L-NbO primary grains are prone to aggregate into secondary particles with a size of several micrometers as shown in Figure 2e and S2a. These primary grains have a sphere-like morphology with a size generally below 100 nm (Figure 2f). Note that these grains can still interconnect with each other even after ultrasonic dispersion treatment for TEM sample preparation (Figure S2b). The good adherence phenomenon should be caused by the high surface energy of defect-rich grain surface. Otherwise, the grains are loosely dispersed and have a size less than 300 nm as shown in the defect-deficient C-NbO (Figure S2c and d). The defect enrichment in L-NbO does not blur the lattice stripes (e.g. with a d-spacing value of 3.92 Å, corresponding to (001) planes, inset of Figure 2f) in high-resolution TEM (HRTEM) image and the diffraction rings in selected area electron diffraction (SAED) pattern (Figure 2g), agreeing with the XRD result. In contrast, the grains of CN-NbO are better defined with a regular short-rod-like morphology in view of the template effect of O-g-C_3N_4, meanwhile the particle aggregation is less serious than L-NbO (Figure 2h and S2e). The potential decrease of grain surface energy in defect-diluted CN-NbO is responsible for the mitigation of particle aggregation. Instead of the direct hydrolysis in water, ethanol is chosen as the solvent of $Nb(Et)_5$, which enables the reduction of nucleation sites and oriented growth of Nb_2O_5 particles with the help of O-g-C_3N_4. One can note that there are some hole regions in the inner of individual CN-NbO grain as observed from HRTEM (Figure 2i, 2j and S2f), leading to the appearance of attenuated and

porous grains, which is beneficial for the electrolyte infiltration and charge/mass transfer in CN-NbO. The inner porosity likely stems from the removal of O-g-C_3N_4 template as Nb^{5+} adsorption supporter during annealing. Figure S3 further compares the morphologies between O-g-C_3N_4 and CN-NbO. The O-g-C_3N_4 template displays the sheet-like monolithic morphology with corrugated surface, favoring the adsorption of Nb^{5+} precursor, its interaction with doped O groups and the following growth of Nb_2O_5 nanoparticles. The volatilization of O-g-C_3N_4 template does not degrade the porous network structure made of numerous Nb_2O_5 nanoparticles linked up to the scale of several micrometers. The preservation of monolithic morphology in CN-NbO confirms the satisfactory template effect.

Electron paramagnetic resonance (EPR) spectroscopy was conducted at room temperature to prove the existence of oxygen vacancies, and the signal originates from the magnetic moment of unpaired electrons. Based on Hund rule, the arrangement of outermost electrons is $4d^45s^1$ for niobium atom. Therefore there is no electron left on the outmost atomic orbitals for Nb^{5+}, and there is one unpaired electron left on the 4d atomic orbital for Nb^{4+}. The unpaired electrons on Nb^{4+} can be attracted and trapped by adjacent O atoms to form oxygen free radicals attached to O vacancies, so that the existence of Nb^{4+} can be proved by EPR signals from oxygen free radicals.[31] From the evolution of EPR curves of C-NbO, L-NbO and CN-NbO in Figure 3a, the signal for L-NbO with a *g* value of 2.0010 is much more intensive than for other samples. With the dilution of O vacancies, the signal for CN-NbO is relatively weak with a *g* value of 2.0013 as shown in the inset. And no distinct EPR peak shows up in the curve of C-NbO, indicating that the annealing step for commercial Nb_2O_5 does not bring in extra O vacancies. Based on the electron spin concentration measurement, the estimated concentrations of free radical $O_2^{\bullet-}$ are 2.29×10^{17} and 7.60×10^{14} for L-NbO and CN-NbO respectively, taking Mn marker as criterion in Figure S4, according to the following formula:

$$\frac{Integral\ area\ of\ standard\ Mn\ peak}{Integral\ area\ of\ Nb_2O_x\ peak} = \frac{3.02\times10^{14}}{m}$$

where m represents the free radical concentration, which is close to the O vacancy concentration. The molar concentrations for L-NbO and CN-NbO are estimated to be 19 μmol/g and 0.31 μmol/g respectively, really close to the data reported in TiO_{2-x}.[18] The EPR result confirms the enrichment and dilution of O vacancies in L-NbO and CN-NbO respectively. We also used the thermogravimetric (TG) analysis to test the oxygen adsorption in L-NbO (Figure S5). Comparing the TG curves of L-NbO in air and N_2, the oxygen absorption is approximately 0.7 wt% based on the weight increase in air. Therefore the x value in T-Nb_2O_{5-x} is estimated to be 0.11 for L-NbO with the formula of $Nb_2O_{4.89}$. Combined with the EPR result, the x value for CN-NbO is expected to be 0.002 with a formula of $Nb_2O_{4.998}$. The TG result should be more reliable than the EPR one in terms of oxygen content, because the magnetic signals of oxygen vacancies easily affect each other for the latter measurement.

To elucidate the element and bonding situations for L-NbO, CN-NbO and C-NbO, their X-ray photoelectron spectra (XPS) are compared. From Nb 3d in Figure 3b, two peaks are observed due to spin-orbit coupling of Nb 3d orbital. The Nb^{5+} $3d_{5/2}$ and Nb^{5+} $3d_{3/2}$ peaks for stoichiometric Nb_2O_5 (i.e. C-NbO) are located at 207.6 and 210.4 eV, with a peak area ratio of 3:2, agreeing with the characteristic positions of Nb^{5+} peaks reported in previous literatures.[32] An overall negatively shift of 0.4 eV for Nb 3d signal can be found for CN-NbO. Luo et al. also observed the similar shift tendency and they ascribed it to the existence of oxygen vacancies.[9] Two smaller peaks at 205.7 and 208.3 eV can be fitted from the curve, corresponding to Nb^{4+} $3d_{5/2}$ and Nb^{4+} $3d_{3/2}$ respectively.[33] However for L-NbO, a positive peak shift of 0.6 eV for Nb^{5+} based on that of C-NbO is observed with two major peaks at 208.2 and 211.0 eV respectively. The similar phenomenon was reported by our previous work on KF doped H-Nb_2O_5.[13] From the evolution of O 1s spectra in Figure 3c, the XPS peaks have the similar shifting tendency as that of niobium. Based on the binding energy (BE) position (531 eV) of the O 1s peak for C-NbO, there is a negative shift of 0.2 eV for CN-NbO and a positive shift of 0.8 eV for L-NbO. Even if the stoichiometric ratio is not much different, the BE value of Nb 3d spectra would vary greatly due to the difference in crystal structure. It is presumed that the positive shift for the BE of Nb is caused by the

enrichment of oxygen defects,[34] which makes the orthorhombic niobium oxide more stable. The introduction of oxygen deficiency alleviates the Jahn-Teller effect and mitigates the structural distortion of NbO_6/NbO_7 polyhedra. In order to further disclose the distortion degree of crystal structure, we calculated the BE difference as a parameter for analysis reported by Atuchin et al.[35] This parameter is defined as the distance difference between the positions of O 1s and cation core levels, namely Δ(O-Nb) = BE (O 1s) – BE (Nb $3d_{5/2}$). The Δ(O-Nb) values for C-NbO, L-NbO and CN-NbO are 323.4, 323.6 and 323.6 eV, respectively. The increase of Δ(O-Nb) value indicates the increase of Nb-O bond length and arrangement of related bonds in Nb_2O_5 structure with the creation of O defects. The specific structural change will be discussed later. Note that, after annealing at 750℃, C_3N_4 is completely extracted from CN-NbO, and therefore no N 1s peak can be distinguished from the XPS result of CN-NbO in Figure 3d. According to the literature,[36] the oxygen content in O-g-C_3N_4 was 6.51% by weight. With annealing temperature increasing, these O atoms doped in C_3N_4 matrix can be released from the matrix and transferred to T-Nb_2O_{5-x} to heal a part of O vacancies.

Raman spectra were used to explore the vibration of metal-oxygen bonds in T-Nb_2O_{5-x}. As shown in Figure 3e, three peaks in 100-400 cm^{-1} are typical bending modes of Nb-O-Nb linkages, which can be observed in both C-NbO and L-NbO. A strong and broad peak at 687 cm^{-1} is observed in the curve of C-NbO, ascribed to the symmetric stretching mode of NbO_6 and NbO_7.[37] In the curve of L-NbO, this peak splits into two peaks at 650 and 722 cm^{-1}. The satellite peak at 650 cm^{-1} is caused by the lengthening of Nb-O bonds due to the existence of oxygen vacancies.[38] To further elucidate the covalent bonds and electronic states in oxygen-defective T-Nb_2O_5, X-ray adsorption near-edge structure (XANES) analysis was adopted (Figure 3f and g). Two almost overlapped curves are observed for L-NbO and CN-NbO, indicating that no distinguished valence difference is induced by oxygen vacancies, consistent with the XPS result. Based on the TG and EPR results, the amount of reduced Nb is very tiny and its content difference between L-NbO and CN-NbO is also not substantial. It is responsible for the difficult discerning of edge shift in their XANES curves. In contrast, the R space curves of Fourier transform spectra for L-NbO and CN-NbO are obviously distinct.

The two peaks below 2.2 Å belong to Nb-O bonds, and the relatively weak three peaks ranging from 2.2 Å to 4 Å are ascribed to the Nb-Nb vectors.[17] It is found that the peak centered at 1 Å for L-NbO displays much lower intensity than that for CN-NbO. The attenuation of this side peak is likely caused by the increase in the centrosymmetry of NbO_x polyhedra.[8] We speculate that the excess oxygen vacancies in L-NbO is favorable for the transformation of tilted pentagonal bipyramids (NbO_7) into titled tetrahedral bipyramids (NbO_6). These vacancies can also alleviate the polyhedron distortion caused by Jahn-Teller effect. The synergistic effect of the two aspects promotes the centrosymmetry of polyhedra. It is deduced that the atomic rearrangement induced by oxygen vacancies loosens the overall atomic framework, indicating the lower steric hindrance for Li migration inside T-Nb_2O_{5-x} particles.

Galvanostatic charge-discharge test was conducted to evaluate the electrochemical performance of defect mediated Nb_2O_5 in a potential range of 0.4-3.0 V, in the electrolyte with $LiPF_6$ dissolved in ethylene carbonate (EC) and dimethyl carbonate (DMC). From the fast charge/discharge curves at 5 C (1C = 200 mA/g) as showed in Figure 4a and S6a, both the L-NbO and CN-NbO anodes display the well-defined intercalation regions around 1.5 V even under such a high rate. The typical T-phase electrochemical profiles are highly duplicated for CN-NbO for at least 1000 cycles, whereas the feature intercalation regions for L-NbO degrade seriously after 500 cycles. From the long cycling performance at 5 C (Figure 4b), CN-NbO shows a ultrastable reversible capacity of 170 mAh/g after 100 cycles, which is still retained at 164 mAh/g after 1100 cycles, whereas L-NbO delivers a much lower value of 110 mAh/g after 1000 cycles. In a sharp contrast, C-NbO shows a rapidly declining capacity below 100 mAh/g after merely 50 cycles. The similar capacity and stability advantages for CN-NbO are also observed when cycled at 0.5 C in Figure 4c. The highly reversible capacity for CN-NbO is as high as 270 mAh/g even after 550 cycles, whereas the corresponding capacity is 200 mAh/g for L-NbO. The introduction of oxygen defects is helpful for the electrical conductivity enhancement and capacity activation with a high coulombic efficiency (CE) of 100%, but the structure stability and absolute capacity of Nb_2O_{5-x} would be in turn influenced if O vacancies are excessive as shown in L-NbO. Note that both L-NbO and

CN-NbO display the higher initial discharge capacities, which are associated with the irreversible formation of lithiated carbon additive and NbO domains in 0.4-3.0 V (Figure S7).[39] These domains are highly conductive and can serve as electron wires to *in-situ* reinforce the electrode network. To clarify the charge storage capacity from carbon, the CB electrodes were fabricated by mixing CB and PVDF in a mass ratio of 9:1. As expected, the initial irreversible capacity of CB is large (~50% contribution of capacity), and it is mainly responsible for the occurrence of irreversible capacity in Li/Nb_2O_{5-x} cells during the first discharge. However the capacity contribution of CB is quite small (~10 %) during the following cycles even under this broader voltage range down to 0.4 V. Reducing the dosage of carbon black during electrode fabrication appears to be an effective method to mitigate the irreversible capacity loss as long as the electronic wiring can be further optimized.

From the rate performance in Figure 4d, 4e and S6b, both the capacities of L-NbO and CN-NbO are obviously higher than those of C-NbO (almost twice as much) at various rates. The CN-NbO electrode delivers the capacities of 292, 256, 216, 187, 144 and 107 mAh/g at 0.5 C, 1.0 C, 2.5 C, 5.0 C, 10 C and 25 C respectively. The capacities of L-NbO at the corresponding rates do not outperform but verge on the capacities of CN-NbO. The rate increase does not seriously degrade the electrochemical reaction profile even though up to 25 C. The narrowing of capacity gap between L-NbO and CN-NbO with rate increase benefits from the higher electron conductivity for the former, which enables a better high-rate tolerability. The better reaction kinetics for L-NbO than CN-NbO also lies in the lower voltage polarization for the former (Figure 4f). Taking the position of capacity at 50% state of charge as criterion, C-NbO, CN-NbO and L-NbO display the potential gap values of 368.3, 220.7 and 173.6 mV respectively at 0.5 C. The intrinsically higher electron conductivity is expected to endow L-NbO with a better electrode thickening effect, which can further improve the areal loading and capacity of electrode. When we stepwise increase the areal loading from 2 to 4 mg/cm^2, L-NbO enables a better capacity retention (than CN-NbO) with a constant capacity of 185 mAh/g (i.e. from 0.38 to 0.74 mAh/cm^2 under 2-4 mg/cm^2) before 100 cycles (Figure 4g and S6c). Its areal capacities are still preserved at 0.36, 0.50 and 0.66 mAh/cm^2 under 2, 3 and 4 mg/cm^2 respectively after 200 cycles. Both the high areal

capacities of 0.74 and 0.65 mAh/cm^2 for L-NbO and CN-NbO are nearly 2-3 times higher than those of other typical anode materials (e.g. commercial $Li_4Ti_5O_{12}$, nanostructured Nb_2O_5 and $Nb_{14}W_3O_{44}$) at the same 100 mA/cm^2 (Figure 4h).[15,26,40] We further compare the relationship between areal current density and areal capacity of our T-Nb_2O_{5-x} with other anode materials without the assistance of *in-situ* conductive wiring in Figure 4i, to emphasize the performance advantage of L-NbO and CN-NbO especially under the conditions of high areal loading and current density.[9, 15, 26, 40-42]

Implantation of oxygen vacancies into MoO_3 was reported to improve the charge storage kinetics and contribute to the pseudocapacitive effect, which is of profound influence on rate performance.[19] CV curves with the scan rates from 0.1 to 2 mV/s were provided to give insight into the role of oxygen vacancies in T-Nb_2O_{5-x}. From the evolution of CV curves of L-NbO and CN-NbO at five different rates in Figure 5a and S8a, an increase of potential hysteresis (with larger redox peak separation ΔE_p) can be observed, proportional to the scan rate. It is obvious that the ΔE_p values for L-NbO are lower than those for CN-NbO at corresponding scan rates (Figure S8b), agreeing with the better rate tolerability for L-NbO during charge/discharge processes. The electrochemical process can be deduced according to the relationship between current and scan rate:

$$i_v = av^b$$

where i_v is the total current, v represents the scan rate in CV, a and b are alterable parameters, which are respectively estimated in accordance with the intercept and slope of the logarithmic form of the above equation:

$$\log i_v = b \log v + \log a$$

The b value is one of criterions to judge the contribution of pseudocapacitive effect in total current. The electrode process is dominated by pseudocapacitive current when the b value approaches 1. On the contrary, when it verges on 0.5, the process is mainly intercalation-controlled. The corresponding fitted line for peak currents can be found in the insets of Figure 5a and S8a. The pseudocapacitive current in L-NbO contributes more to total

charge storage with the b values of 0.787 and 0.794 for anodic and cathodic peaks respectively, and the b values for CN-NbO are around 0.6. The measured current can be divided into pseudocapacitive current and intercalation current, which can be calculated quantitatively via the following formula:

$$i_v = k_1 v + k_2 v^{1/2}$$

$$\text{namely, } i_v/v^{1/2} = k_1 v^{1/2} + k_2$$

where $k_1 v$ and $k_2 v^{1/2}$ are assigned to pseudocapacitive and intercalation current contributions respectively.[43] k_1 and k_2 can be calculated by the slope and intercept of transformed formula, a linear function between $i_v/v^{1/2}$ and $v^{1/2}$. A typical CV curve with conformal capacitive area outlining the pseudocapacitive current (orange area) at 0.5 mV/s can be found in Figure 5b. From the stacked columns of intercalated (gray section) and pseudocapacitive (colored section) current contributions in Figure 5c, L-NbO shows the higher pseudocapacitive percentages (e.g. 81% at 2 mV/s) than CN-NbO (65%) at all the rates. Since the particle sizes are comparable for L-NbO and CN-NbO, the more remarkable pseduocapacitive effect for the former is thought to be highly associated with its rich oxygen vacancies and resultant higher electron conductivity.[19,44]

Li^+ diffusion coefficient is proportional to the slope of fitted line of the relationship between peak current vs. square root of scan rate presented in Figure 5d. Impressively, the peak currents of L-NbO in CV curves are higher than those of CN-NbO at corresponding rates, indicating the higher diffusion coefficient for L-NbO (4.97×10^{-13} cm^2/s vs. 4.40×10^{-14} cm^2/s for CN-NbO, see the calculation details in Figure S8). Galvanostatic intermittent titration technique (GITT) analysis is used to further estimate Li^+ diffusion coefficient (D_{Li^+}) at different state of charge (Figure 5e, S9a and b). The D_{Li^+} value is calculated based on the following formula according to the second Fick's law of diffusion:

$$D_{Li^+} = \frac{4}{\pi}\left(\frac{mV_m}{MS}\right)^2\left(\frac{\Delta E_s}{\tau\left(\frac{dE_\tau}{d\sqrt{\tau}}\right)}\right)^2 \left(\tau \ll \frac{l^2}{D_{Li^+}}\right)$$

where m, V_m and M refer to the mass loading, molar volume (50.7 cm^3/mol) and molecular weight (265.81 g/mol), and l and S are the thickness and surface area (0.503×10^{-4} m^2) of active material respectively.[43] τ is the period of intermittent charge and discharge, equal to 3600 s, ΔE_s represents the open-circuit potential gap after two adjacent relexation processes and E_τ is the transient potential during charge and discharge, as shown in Figure S9c and d. There is obvious linear relationship between E_τ and $\sqrt{\tau}$ for L-NbO and CN-NbO (Figure S9e and f). Therefore, the above formula can be simplified:

$$D_{Li^+} = \frac{4}{\pi\tau}\left(\frac{mV_m}{MS}\right)^2\left(\frac{\Delta E_s}{\Delta E_\tau}\right)^2\left(\tau \ll \frac{l^2}{D_{Li^+}}\right)$$

We attempted different relaxation times (6 h, 12 h and 24 h) during GITT. Unfortunately, even if the relaxation time is extended to 24 h, the equilibrium state is still not reached for the discharge process. On the contrary, the equilibrium state is reached within 6 h in the charge process (Figure S9c). Therefore we adopted a relaxation time of 6 h for the analysis of diffusion coefficients for the charge process. The reaction-potential-dependent D_{Li^+} for L-NbO mainly ranges from 7.27×10^{-13} to 5.65×10^{-13} cm^2/s in the most of states of charge (SOC) from 20% to 80%, which is higher than that of CN-NbO (from 6.91×10^{-13} to 9.11×10^{-14} cm^2/s) and C-NbO (from 3.74×10^{-13} to 7.64×10^{-14} cm^2/s) in the corresponding SOC range (Figure 5f). With the increase of delithiation depth, the diffusion coefficients for L-NbO are more stable than those for CN-NbO and C-NbO, benefiting from the more supply of electron density in L-NbO. Note that, under the GITT mode, the pre-cycled L-NbO can be easily discharged to the terminated voltage of 0.4 V, while there is a long tail in the discharge curves of C-NbO and CN-NbO. These phenomena are associated with the polarization overpotential (i.e. the difference between cutoff voltage and open-circuit voltage after relaxation), further signifying the better kinetics of L-NbO. From Figure S9g and h, the overpotential values are lowest for L-NbO especially at the deep discharge stages, and they are as small as 35.6 and 13.3 mV at the 50% SOD and SOC respectively.

The potential hysteresis between the anodic and cathodic peaks in CV curves becomes larger with the increase of scan rate. And the curves in the scope of 2.5-2.0 V in the cathodic

sweep (Figure 5a) overlap with each other. This regular evolution is consistent with the theoretical CV curves calculated from the slow nucleation control process reported by Nikitina et al.[45] It is assumed that the Li intercalation in the low overpotential area is dominated by slow nucleation step and the similar phenomenon was reported in V_2O_5.[46] Potentiostatic intermittent titration technique (PITT) was used to characterize the nucleation of $Li_yNb_2O_{5-x}$ phases from 2.5 to 1.5 V during discharge (Figure S10). The potential gap between continuous steps is 0.05 V and the duration of every step is 1800 s. The obtained linear relationship between the logarithmic function of current (ln(I)) in potentiostatic state and the resting time (in Region III) is the most powerful diagnostic criteria of the diffusive nucleation control.[46] Unlike the transformation between Li-poor and Li-rich phases in $LiFePO_4$, there is no well-defined transformation to slow nucleation rate-control region (Region II) in T-Nb_2O_{5-x} (Figure S11a).[47] The plots of nucleation rates (K_{nucl}) as a function of discharge potential, equal to the slope of ln(I) vs. time (t) in Region III based on the equation $\ln(I) = -K_{nucl}\, t + \text{const}$, indicates that the K_{nucl} values of CN-NbO outperform those of L-NbO in the discharge process (Figure S11b). Note that oxygen vacancies as nucleation sites are prone to capture Li^+, and they can be faster saturated in Region I and II at a certain potential for L-NbO. The faster electrochemical healing of nucleation sites leads to a significant drop of nucleation rate in Region III for L-NbO. With the deepening of discharge, the nucleation sites are further diluted, and the K_{nucl} value correspondingly increases. The charge quantity is calculated from the integral of the current-time curve. The higher charge quantity for L-NbO during each PITT step is an auxiliary evidence for the better kinetics of L-NbO (Figure S11c).

Oxygen vacancies inside T-Nb_2O_{5-x} are favorable for the earlier formation of metallic $Li_yNb_2O_{5-x}$, and these vacancies on particle surface likely interfere with the formation of SEI. Therefore electrochemical impedance spectroscopy (EIS) was used to characterize the interfacial resistance. Figure 5g and S12a-c display the Nyquist plots of Li/L-NbO and Li/CN-NbO cells at different temperatures before cycling and after 5 cycles, which are well fitted with equivalent circuit in the insets. The nearly complete semicircle at high frequencies is assigned to the SEI resistance (R_{SEI}), and the incomplete semicircle at medium frequencies

corresponds to the charge transfer (CT) resistance (R_{CT}). The inclined straight line at low frequencies is associated with a finite-length Warburg impedance (Z_{flw}), denoting both diffusion and accumulation of Li^+.[48] The intercept before the starting of Nyquist curves on the real axis refers to the resistance of internal electrolyte (R_E). After cycling for 5 cycles, there is no obvious change on R_E for both L-NbO and CN-NbO, which ranges from 5 to 8 Ω dependent on the testing temperature. SEI layer plays a pivotal role in the electrochemical process, associated with the desolvation and migration of Li^+. As showed in Figure S12d and e, L-NbO displays the higher SEI resistance than CN-NbO from 30 to 60℃ before cycling, but with comparable activation energies (E_a) for R_{SEI}. It indicates that richer O defects at L-NbO surface may catalyze the electrolyte decomposition and its passivation effect. After 5 cycles, the opposite trend appears for SEI resistance, and the R_{SEI} values become smaller for L-NbO than for CN-NbO (Figure S12f). The E_a value for L-NbO (0.684 eV vs. 0.702 eV for CN-NbO) is also correspondingly lower (Figure 5h). The Li trapping in rich-defect-sites is expected to enable the formation of more conductive SEI containing metallic $Li_yNb_2O_{5-x}$ phase, which is responsible for the lower R_{SEI} and E_a for cycled L-NbO. The E_a value for R_{CT} is also smaller for L-NbO (0.306 eV) than for CN-NbO (0.380 eV) after 5 cycles (Figure 5i and S12g).

To deeply elucidate the roles of oxygen vacancies inside T-Nb_2O_{5-x}, density function theory (DFT) calculation was used to unveil the possible vacancy locations and structure evolution. As reported by Liu et. al.,[49] there are two different types of oxygen atoms. The calculation unit is observed in Figure S13a, where the structure is composed of alternating 4g layer (loosely packed layer, O atomic coordinate: x, y, 0) and 4h layer (densely packed layer, O atomic coordinate: x, y, 1/2) in Figure S13b and S13c respectively. Combining with the proposed oxygen-vacancy-formation mechanism,[27] we deduce that oxygen vacancies are more likely to be formed at the positions of bridged oxygen atoms, namely the oxygen atoms in 4g layers (Position 1). It is also possible that oxygen atoms can be removed from 4h layers, e.g. the detachment of O atoms from Position 2 (with coordination number of 4 with Nb atoms) or Position 3 (with coordination number of 3 with Nb atoms). As showed in Figure 6a, three typical oxygen atoms are considered to detach from T-Nb_2O_5 framework in order to

construct different defect structures. After removing the apical oxygen atom of NbO_6 on Position 1, a small migration of Nb atom around c axis occurs as observed in Figure 6b and c. The assignment of niobium-oxygen polyhedron to NbO_6 or NbO_7 is determined by the coordination number of Nb atom, that is, the number of O atoms closest to the Nb atom. Since Nb-O is a covalent bond, which cannot be formed when the distance between Nb and O exceeds a threshold value of 2.3 Å.[50] The Nb-O bond lengths in our model are in the scope of 1.9-2.3 Å. After the introduction of O vacancies in Position 1, the situation of Nb-O bond length in the unit cell changes. In the pristine T-Nb_2O_5 structure, the Nb-O bonds originally exist at the two arrows (Figure 6b). But these bonds are broken after vacancy introduction due to the increase of distance between Nb and O to 2.50 Å and 2.78 Å (beyond the threshold 2.30 Å). So a part of original NbO_7 motifs is transformed into NbO_6 ones. The Position 2 and 3 denote the O atoms at the common vertex and common edge junction of NbO_x polyhedra around the level of Nb atomic layer respectively. There is no obvious structural change after extracting the O atoms from Position 2 or 3, but the NbO_7 pentagonal bipyramids near the corresponding O vacancies are prone to be transformed into NbO_6 tetragonal bipyramids (Figure S14).

We tested the adsorption spectra of L-NbO and C-NbO in the scope of 300-2100 nm to estimate their band gaps (Figure 6e and f), which can further indicate the preference of O vacancy position. C-NbO displays a sharp absorption edge around 400 nm, corresponding to the ultraviolet region. This absorption is ascribed to the electronic transition from valence band to conduction band. In sharp contrast, L-NbO exhibits a dramatic light absorption in the ultraviolet-visible-infrared area and no distinct absorption edge is observed. The enhanced light absorption in the visible-infrared area is ascribed to the existence of Nb^{4+} and oxygen vacancies, which indicates the additional manner of electronic transition with reduced energy barrier.[51] The band gaps obtained from Tauc plots derived from absorption curves are 3.23 and 2.30 eV for C-NbO and L-NbO respectively. The obvious descending trend of band gap caused by the extra introduction of oxygen vacancies is consistent with the following calculation result. Partial density of state (PDOS) was employed to reveal the electrical conductivity derived from different oxygen defect structures.[52] As shown in Figure 6d,

T-Nb_2O_{5-x} with oxygen vacancies on Position 1 has a bandgap of 1.365 eV, much lower than that of pristine T-Nb_2O_5 (1.844 eV). In comparison, T-Nb_2O_{5-x} with oxygen vacancies on Position 2 and 3 displays the approximate bandgaps with that of pristine T-Nb_2O_5. Therefore, the oxygen vacancies inside T-Nb_2O_{5-x} are likely located at Position 1, namely the bridging oxygen atom positions between two adjacent NbO_x polyhedral layers. Note that there is a gap between the experimental data and calculation result, which is ascribed to two aspects. On the one hand, the calculation unit of T-Nb_2O_5 is simplified compared with the pristine structure of T-Nb_2O_5 in Figure 2b. On the other hand, we did not use the Dudarev + U correction in this simulation, and the similar treatment has been widely used in previous reports.[53,54] They also reported a lowered band gap of ~ 2 eV if without the consideration of U value, which is very close to our value (~1.8 eV). The band gap is expected to gradually increase with the increase of U value. The calculated PDOS of T-Nb_2O_5 shows that valence band is mainly composed of O 2p and Nb 4p orbitals, while the conduction band is mainly composed of Nb 3d orbitals. We speculate that the electrons triggered by O vacancies at Position 2 and 3 are prone to be confined in nearby Nb-O bonds (with better stability than those in the case of Position 1) in the 4h layer and are difficult to be captured by Nb 3d orbitals, likely responsible to the negligible shrinkage of band gap in the cases of Position 2 and 3.[55] Combined with the experiment of adsorption spectra, it can be deduced that the O atom extraction in T-Nb_2O_{5-x} should occur at Position 1.

Recently, a rocking-chair battery-supercapacitor hybrid device was assembled by taking T-Nb_2O_5 as anode and $LiNi_{0.815}Co_{0.15}Al_{0.035}O_2$ (NCA) as cathode, achieving an energy density of 83Wh/kg within a cycle of 33 s.[56] However this Nb_2O_5/NCA full cell displays the capacities much below 100 mAh/g from 0.05 to 5 A/g. To testify the practical availability of our T-Nb_2O_{5-x}, we assembled the full cells with prelithiated L-NbO as anode and $LiNi_{0.8}Co_{0.1}Mn_{0.1}O_2$ (NCM811) as cathode. Both the anode and cathode can deliver the almost equal capacity of approximately 250 mAh/g at 200 and 140 mA/g, respectively (Figure 6g). We used the integral area (potential vs. specific capacity) to estimate the average voltage during both the charging and discharging processes for Li/L-NbO and Li/NCM811 half cells (Figure S15). The average voltages of L-NbO and NCM811 are estimated to be

1.42 V for lithiation and 3.96 V for delithiation respectively. Therefore the expected average voltage of L-NbO/NCM811 full cell is estimated to be 2.54 V during the charge process. For the delithiation of L-NbO and lithiation of NCM811, their average voltages are estimated to be 1.81 V and 3.85 V respectively, leading to an expected average voltage of 2.04 V for the discharge of L-NbO/NCM811 full cell. On the other hand, the practical average voltages of L-NbO/NCM811 full cell are estimated to be 2.21 V and 2.01 V for the charge and discharge processes respectively, close to the expected values (Figure 6h). The L-NbO/NCM811 full cell delivers the capacities of 229, 215, 189, 150 and 86 mAh/g at 0.2, 0.5, 1.0, 2.0 and 5.0 C respectively (Figure 6i). The capacity reversibly recovers to 212 mAh/g when the rate skips back to 0.5 C. The characteristic charge/discharge curves of full cell can be well preserved even under high rates exceeding 2 C. The excellent cycling stability of full cell can be observed in Figure 6j, with an average decaying rate of 0.19 % after 110 cycles at 0.5 C.

CONCLUSION

In summary, we introduce oxygen vacancies into T-Nb_2O_5 through acid immersion of amorphous $Nb_2O_5 \cdot nH_2O$. The enrichment of oxygen vacancies contributes to the remarkable improvement of electric conductivity (6.752×10^{-5} S/cm), Li diffusion coefficient (10^{-12}-10^{-13} cm^2/s), intercalation pseudocapacitive effect (81% at 2 mV/s) and kinetic indexes (from GITT, PITT and EIS) for L-NbO. DFT calculation reveals that the bridged oxygen atoms between NbO_x polyhedra layers are more likely to be detached from lattices with a descending bandgap. The better rate tolerability for L-NbO (96 mAh/g at 25 C) enables a stable cycling performance with a high areal capacity of 0.74 mAh/cm^2 (after 100 cycles) even under high mass loading of 4 mg/cm^2. The further employment of O-doped g-C_3N_4 template as trace oxygen pump opens a new avenue to heal excess oxygen vacancies in T-Nb_2O_{5-x} and promote the formation of monolithic electrode network. Defect concentration of CN-NbO is reduced to about 1/60 of that of L-NbO. Defect-mitigated CN-NbO displays extraordinary cycling stability (164 mAh/g at 5 C after 1100 cycles) and capacity retention (104 mAh/g) at ultrahigh rate (25 C). Considering the prominent electrochemical

performance of our Nb_2O_{5-x}/NCM811 full cells, oxygen-defect modulation strategy on oxide anodes provides alternative solution to fast-charging and durable LIBs.

Supporting Information

Supplementary information is available for this paper at https://doi.org/

Acknowledgements

This work was supported by National Key R&D Program of China (2016YFB0901600), NSAF (Grant No. U1830113), National Natural Science Foundation of China (51772313 and 21975276), and Shanghai Science and Technology Committee (20520710800). This research used the resources at Beamline 7-BM (QAS) of the National Synchrotron Light Source II, a U.S. Department of Energy (DOE) Office of Science User Facility operated for the DOE Office of Science by Brookhaven National Laboratory under Contract No. DE-SC0012704.

References

[1] Y. Liu, Y. Zhu, Y. Cui, *Nat. Energy* **2019**, *4*, 540.

[2] J. Deng, C. Bae, A. Denlinger, T. Miller, *Joule* **2020**, *4*, 511.

[3] T.-F. Yi, S.-Y. Yang, Y. Xie, *J. Mater. Chem. A* **2015**, *3*, 5750.

[4] Z. Liu, W. Dong, J. Wang, C. Dong, Y. Lin, I. W. Chen, F. Huang, *iScience* **2020**, *23*, 100767.

[5] P. F. Yu, C. L. Li, X. X. Guo, *J. Phys. Chem. C* **2014**, *118*, 10616.

[6] K. J. Griffith, A. C. Forse, J. M. Griffin, C. P. Grey, *J. Am. Chem. Soc.* **2016**, *138*, 8888

[7] Z. Song, H. Li, W. Liu, H. Zhang, J. Yan, Y. Tang, J. Huang, H. Zhang, X. Li, *Adv. Mater.* **2020**, *32*, 2001001.

[8] V. Augustyn, J. Come, M. A. Lowe, J. W. Kim, P. L. Taberna, S. H. Tolbert, H. D. Abruna, P. Simon, B. Dunn, *Nat. Mater.* **2013**, *12*, 518.

[9] L. Yan, G. Chen, M. Zhou, H. Luo, *ECS Trans.* **2015**, *66*, 277.

[10] H. T. Sun, L. Mei, J. F. Liang, Z. P. Zhao, C. Lee, H. L. Fei, M. N. Ding, J. Lau, M. F. Li, C. Wang, X. Xu, G. L. Hao, B. Papandrea, I. Shakir, B. Dunn, Y. Huang, X. F. Duan, *Science* **2017**, *356*, 599.

[11] J. Meng, Q. He, L. Xu, X. Zhang, F. Liu, X. Wang, Q. Li, X. Xu, G. Zhang, C. Niu, Z. Xiao, Z. Liu, Z. Zhu, Y. Zhao, L. Mai, *Adv. Energy Mater.* **2019**, *9*, 1802695.

[12] J. Y. Cheong, C. Kim, J. W. Jung, K. R. Yoon, S. H. Cho, D. Y. Youn, H. Y. Jang, I. D. Kim, *Small* **2017**, *13*, 1603601.

[13] D. Cao, Z. Yao, J. Liu, J. Zhang, C. Li, *Energy Storage Mater.* **2018**, *11*, 152.

[14] Y. Han, M. Yang, Y. Zhang, J. Xie, D. Yin, C. Li, *Chem. Mater.* **2016**, *28*, 3139.

[15] Y. Yang, H. Zhu, J. Xiao, H. Geng, Y. Zhang, J. Zhao, G. Li, X. L. Wang, C. C. Li, Q. Liu, *Adv. Mater.* **2020**, *32*, 1905295.

[16] L. Yang, X. Zhu, X. Li, X. Zhao, K. Pei, W. You, X. Li, Y. Chen, C. Lin, R. Che, *Adv. Energy Mater.* **2019**, *9*, 1902174.

[17] S. J. Deng, H. Zhu, G. Z. Wang, M. Luo, S. H. Shen, C. Z. Ai, L. Yang, S. W. Lin, Q. H. Zhang, L. Gu, B. Liu, Y. Zhang, Q. Liu, G. X. Pan, Q. Q. Xiong, X. L. Wang, X. H. Xia, J. P. Tu, *Nat. Commun.* **2020**, *11*, 11.

[18] Y. R. Wang, X. L. Xue, P. Y. Liu, C. X. Wang, X. Yi, Y. Hu, L. B. Ma, G. Y. Zhu, R. P. Chen, T. Chen, J. Ma, J. Liu, Z. Jin, *ACS Nano* **2018**, *12*, 12492.

[19] H. S. Kim, J. B. Cook, H. Lin, J. S. Ko, S. H. Tolbert, V. Ozolins, B. Dunn, *Nat. Mater.* **2017**, *16*, 454.

[20] T. Xiong, Z. G. Yu, H. Wu, Y. Du, Q. Xie, J. Chen, Y. W. Zhang, S. J. Pennycook, W. S. V. Lee, J. Xue, *Adv. Energy Mater.* **2019**, *9*, 1803815.

[21] P. V. Sushko, K. M. Rosso, J.-G. Zhang, J. Liu, M. L. Sushko, *Adv. Funct. Mater.* **2013**, *23*, 5530.

[22] Y. Zhang, Z. Ding, C. W. Foster, C. E. Banks, X. Qiu, X. Ji, *Adv. Funct. Mater.* **2017**, *27*, 1700856.

[23] S. Zhang, G. Liu, W. Qiao, J. Wang, L. Ling, *J Colloid Interface Sci* **2020**, *562*, 193.

[24] A. Naldoni, M. Allieta, S. Santangelo, M. Marelli, F. Fabbri, S. Cappelli, C. L. Bianchi, R. Psaro, V. Dal Santo, *J. Am. Chem. Soc.* **2012**, *134*, 7600.

[25] H. Zhang, B. M. May, F. Omenya, M. S. Whittingham, J. Cabana, G. Zhou, *Chem. Mater.* **2019**, *31*, 7790.

[26] L. Yan, G. Chen, S. Sarker, S. Richins, H. Wang, W. Xu, X. Rui, H. Luo, *ACS. Appl. Mater. Interface* **2016**, *8*, 22213.

[27] H. T. Kreissl, M. M. J. Li, Y. K. Peng, K. Nakagawa, T. J. N. Hooper, J. V. Hanna, A. Shepherd, T. S. Wu, Y. L. Soo, S. C. E. Tsang, *J. Am. Chem. Soc.* **2017**, *139*, 12670.

[28] L. Peng, P. Xiong, L. Ma, Y. Yuan, Y. Zhu, D. Chen, X. Luo, J. Lu, K. Amine, G. Yu, *Nat. Commun.* **2017**, *8*, 10.

[29]Y. Yuan, L. Zhang, J. Xing, M. I. B. Utama, X. Lu, K. Du, Y. Li, X. Hu, S. Wang, A. Genç, R. Dunin-Borkowski, J. Arbiol, Q. Xiong, *Nanoscale* **2015**, *7*, 12343.

[30] K. Martin, I. D. Brown., *J. Solid State Chem.* **1994**, *115*, 12.

[31] H. He, D. Huang, W. Pang, D. Sun, Q. Wang, Y. Tang, X. Ji, Z. Guo, H. Wang, *Adv. Mater.* **2018**, *30*, 1801013.

[32] H. L. Cui, G. L. Zhu, Y. Xie, W. Zhao, C. Y. Yang, T. Q. Lin, H. Gu, F. Q. Huang, *J. Mater. Chem. A* **2015**, *3*, 11830.

[33] T. C. Canevari, L. T. Arenas, R. Landers, R. Custodio, Y. Gushikem, *Analyst* **2013**, *138*, 315.

[34] K. Kim, M.-S. Kim, P.-R. Cha, S. H. Kang, J.-H. Kim, *Chem. Mater.* **2016**, *28*, 1453.

[35] V. V. Atuchin, J. C. Grivel, A. S. Korotkov, Z. Zhang, *J. Solid State Chem.* **2008**, *181*, 1285.

[36] X. She, J. Wu, J. Zhong, H. Xu, Y. Yang, R. Vajtai, J. Lou, Y. Liu, D. Du, H. Li, P. M. Ajayan, *Nano Energy* **2016**, *27*, 138.

[37] J. M. Jehng, I. E. Wachs, *Chem. Mater.* **1991**, *3*, 100.

[38] F. D. Hardcastle, I. E. Wachs, *Solid State Ionics* **1991**, *45*, 13.

[39] H. Kim, E. Lim, C. Jo, G. Yoon, J. Hwang, S. Jeong, J. Lee, K. Kang, *Nano Energy* **2015**, *16*, 62.

[40]D. Wang, H. Liu, Z. Shan, D. Xia, R. Na, H. Liu, B. Wang, J. Tian, *Energy Storage Mate r.* **2020**, *27*, 387

[41] S. Q. Guo, X. Zhang, Z. Zhou, G. D. Gao, L. Liu, *J. Mater. Chem. A* **2014**, *2*, 9236.

[42] Z. Ma, X. Gao, Z. She, M. A. Pope, Y. Li, *ChemElectroChem* **2020**, *7*, 4124.

[43] J. Tian, D. Cao, X. Zhou, J. Hu, M. Huang, C. Li, *ACS Nano* **2018**, *12*, 3424.

[44] Z. G. Yao, Q. P. Wu, K. Y. Chen, J. J. Liu, C. L. Li, *Energy Environ. Sci.* **2020**, *13*, 3149.

[45] S. Y. Vassiliev, E. E. Levin, D. E. Presnov, V. A. Nikitina, *J. Electrochem. Soc.* **2019**, *166*, 829.

[46] V. A. Nikitina, S. Y. Vassiliev, K. J. Stevenson, *Adv. Energy Mater.* **2020**, *10*, 1903933.

[47] C. Delacourt, P. Poizot, J.-M. Tarascon, C. Masquelier, *Nat. Mater.* **2005**, *4*, 254.

[48] P. Wang, J. Tian, J. Hu, X. Zhou, C. Li, *ACS Nano* **2017**, *11*, 7390.

[49] D. C. Chen, J. H. Wang, T. F. Chou, B. T. Zhao, M. A. El-Sayed, M. L. Liu, *J. Am. Chem. Soc*. **2017**, *139*, 7071.

[50]B. Cordero, V. Gómez, A. E. Platero-Prats, M. Revés, J. Echeverría, E. Cremades, F. Barragán, S. Alvarez, *Dalton Trans.* **2008**, *21*, 2832.

[51]Y. Wang, X. H. Liu, Q. Wang, M. Quick, S. A. Kovalenko, Q. Y. Chen, N. Koch, N. Pinna, *Angew. Chem. Int. Ed.* **2020**, *59*, 7748.

[52] Z. Ma, K. Rui, Y. Zhang, D. Li, Q. Wang, Q. Zhang, M. Du, J. Yan, C. Zhang, X. Huang, J. Zhu, W. Huang, *Small* **2019**, *15*, 1900583.

[53]
M. B. Pinto, A. L. Soares, A. Mella Orellana, H. A. Duarte, H. A. De Abreu, *J. Phys. Chem. A* **2017**, *121*, 2399.

[54]
Y. Jia, M. Zhong, F. Yang, C. Liang, H. Ren, B. Hu, Q. Liu, H. Zhao, Y. Zhang, Y. Zhao, *J. Phys. Chem. C* **2020**, *124*, 15066.

[55] F. Crasto de Lima, A. Fazzio, *Phys. Chem. Chem. Phys.* **2021**, *23*, 11501.

[56] F. Su, J. Q. Qin, P. Das, F. Zhou, Z. S. Wu, *Energy Environ. Sci.* **2021**, *14*, 2269.

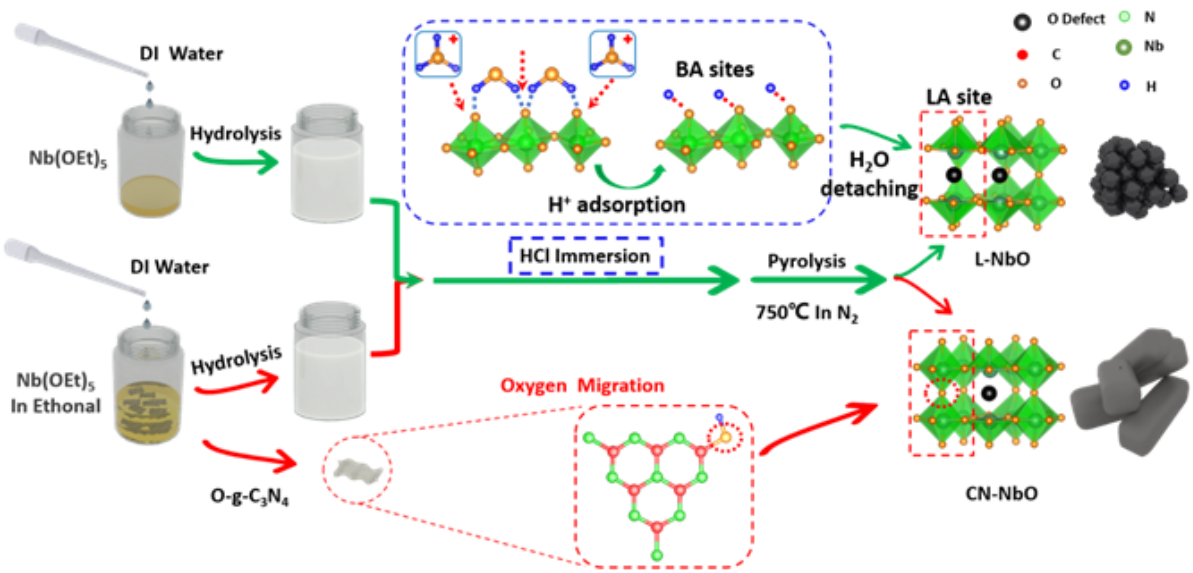

Figure 1. Schematic illustration of synthetic steps of T-Nb_2O_{5-x}, including vacancy formation process and oxygen migration process from O-g-C_3N_4 to T-Nb_2O_{5-x}.

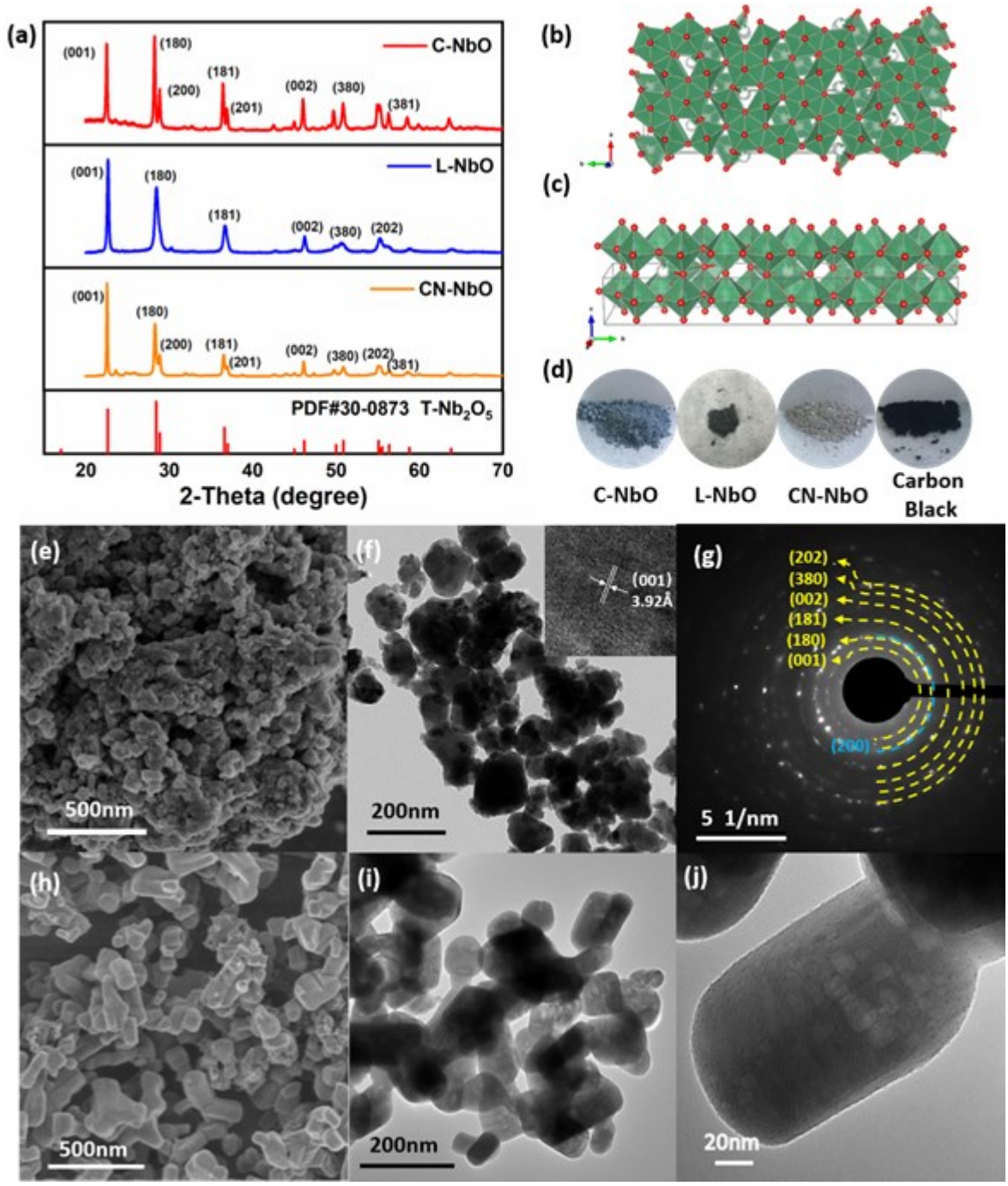

Figure 2. (a) XRD curves of C-NbO, L-NbO and CN-NbO. Layered structure of T-Nb_2O_5 with the views along (b) c axis and (c) a axis. (d) Digital pictures of C-NbO, L-NbO, CN-NbO and carbon black powders. (e) SEM and (f) TEM images of L-NbO. Inset: HRTEM image of L-NbO. (g) SAED pattern of L-NbO. (h) SEM and (i, j) TEM images of CN-NbO in different scales.

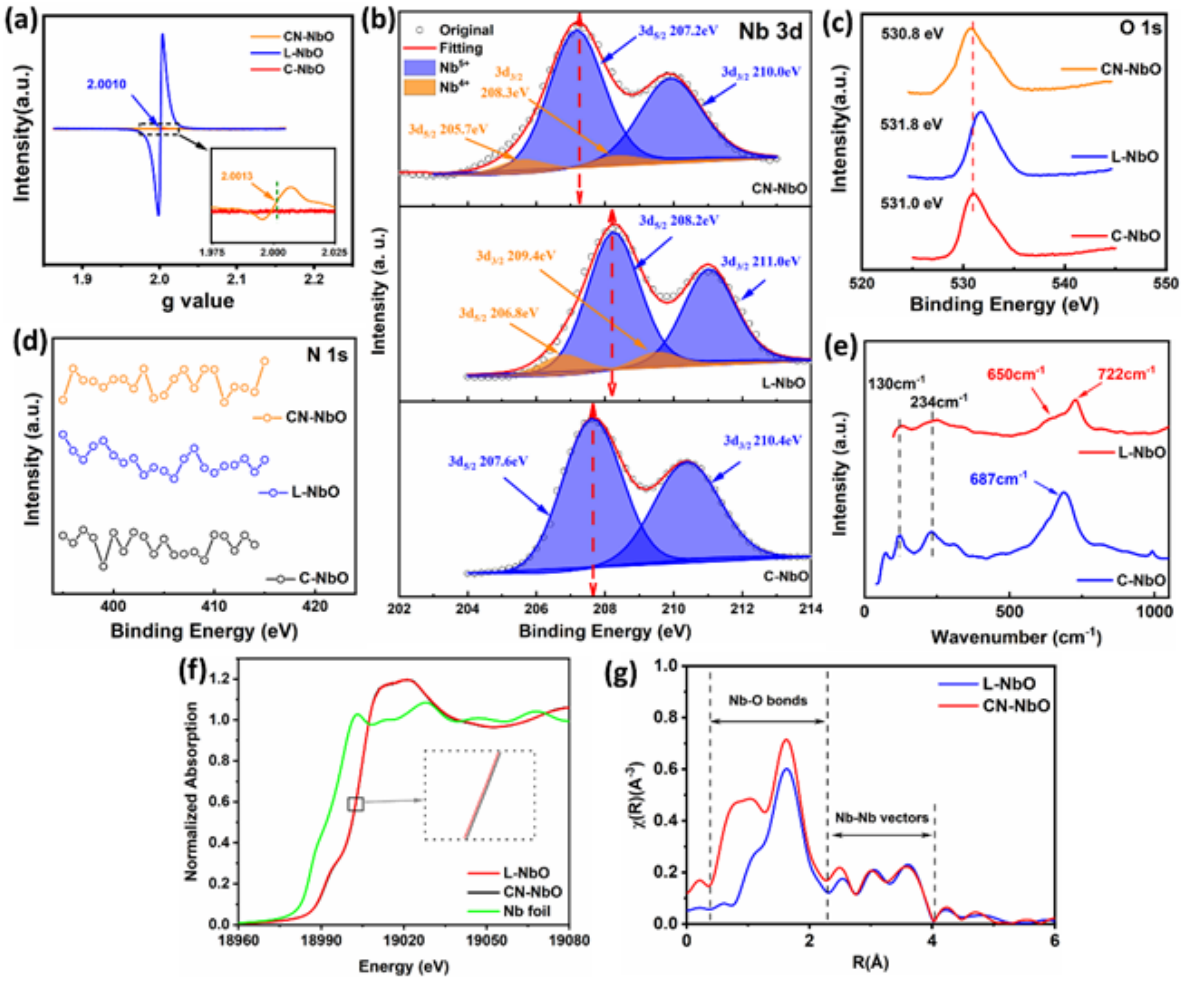

Figure 3. (a) EPR curves for CN-NbO, L-NbO and C-NbO. Inset: magnified EPR curve for CN-NbO. XPS spectra of (b) Nb 3d , (c) O 1s , (d) N 1s for CN-NbO, L-NbO and C-NbO. (e) Raman spectra of L-NbO and C-NbO. (f) Nb K-edge XANES of L-NbO and CN-NbO. (g) Fourier-transformed Nb K-edge XANES of L-NbO and CN-NbO.

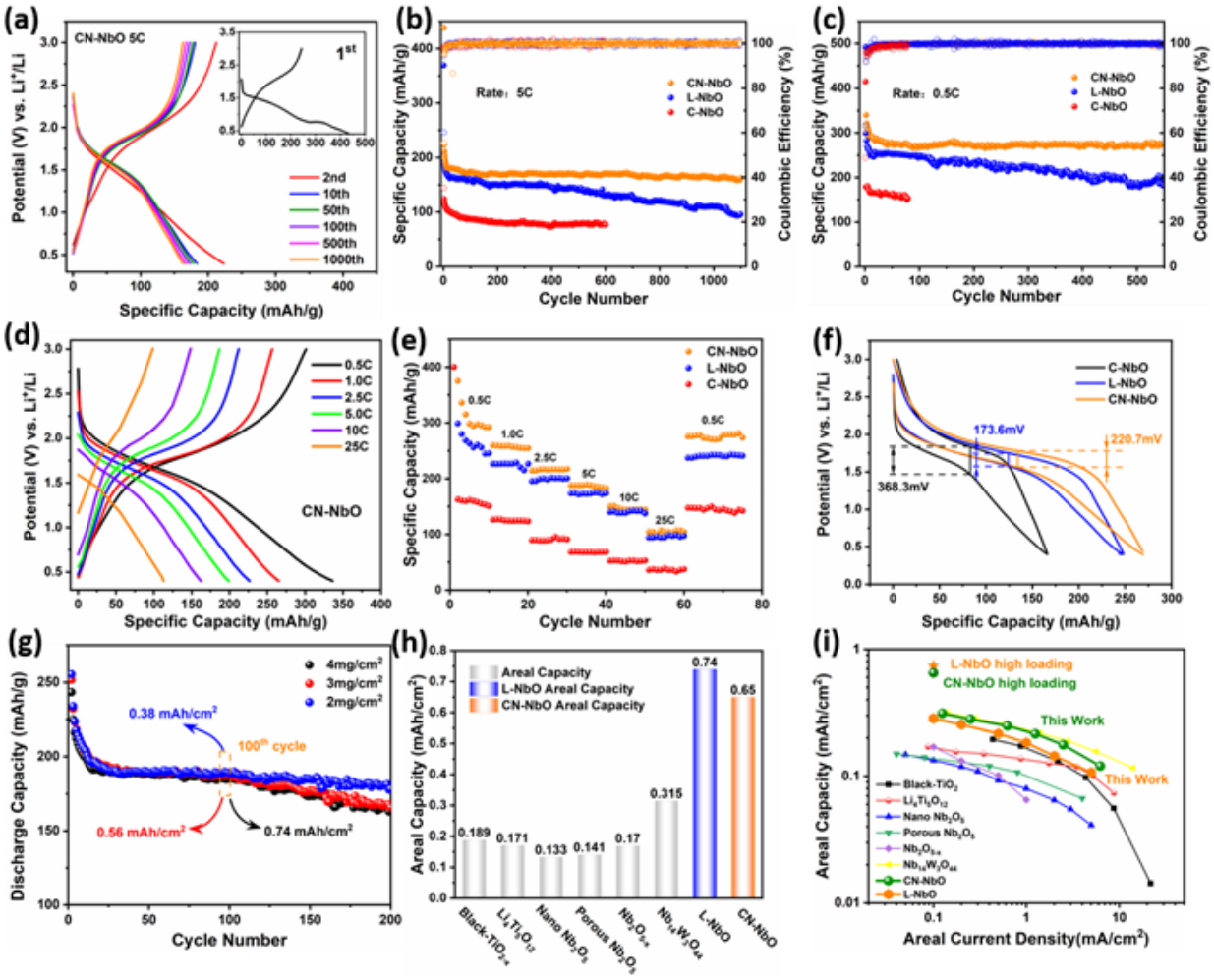

Figure 4. (a) Charge/discharge curves of Li/CN-NbO cell at 5 C at different cycling stages. Inset: charge/discharge curves of CN-NbO during the first cycle. Cycling performance comparison of Li/CN-NbO, Li/L-NbO and Li/C-NbO cells at (b) 5 C and (c) 0.5 C. (d) Charge/discharge curves for Li/CN-NbO cell at various rates from 0.5 C to 25 C. (e) Rate performance comparison of Li/CN-NbO, Li/L-NbO and Li/C-NbO cells from 0.5 C to 25 C. (f) Polarization gap between charge/discharge curves at 50% state of discharge for C-NbO, L-NbO and CN-NbO. (g) Cycling performance of Li/L-NbO cells with high areal loading of 2, 3 and 4 mg/cm^2 at 0.5 C. (h) Column chart of areal capacity values at 100 mA/g for L-NbO, CN-NbO and other reported oxide anode materials. (i) Plots of areal capacity as a function of areal current density for L-NbO, CN-NbO and other typical oxide anode materials.

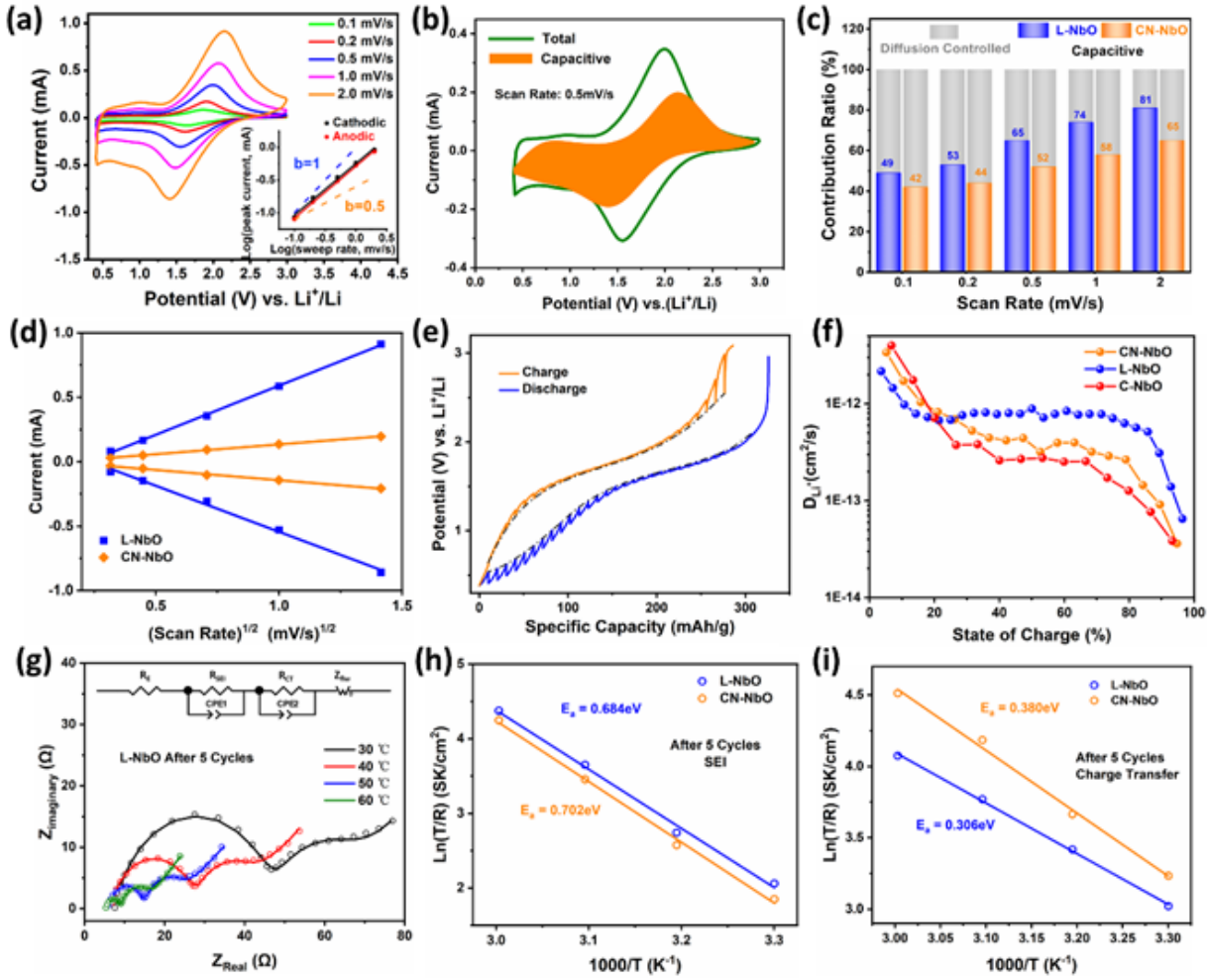

Figure 5. (a) CV curves of L-NbO from 0.1 to 2.0 mV/s. Inset: power law dependence of peak current on corresponding scan rate based on: $\log i(V) = b \log v + \log a$. (b) Profile of calculated pseudocapacitive current ($k_1 v$) based on $i(V) = k_1 v + k_2 v^{1/2}$ at 0.5 mV/s for L-NbO. (c) Column graphs of pseudocapacitive contribution percentage in total current at various scan rates from 0.1 to 2 mV/s for L-NbO and CN-NbO. (d) Scatter plots and fitted linearity of peak current vs. square root of scan rate for L-NbO and CN-NbO. (e) GITT curves of charge/discharge process for L-NbO. (f) Li^+ diffusion coefficient plots estimated by GITT as a function of state of charge for C-NbO, L-NbO and CN-NbO. (g) Nyquist plots at 30-60 ℃ for Li/L-NbO cell after 5 cycles at 0.5 C. Inset: equivalent circuit to simulate Nyquist plots. Arrhenius plots ($\ln T/R$ vs. 1000/T) of (h) SEI resistance and (i) charge transfer resistance for Li/L-NbO and Li/CN-NbO cells after 5 cycles.

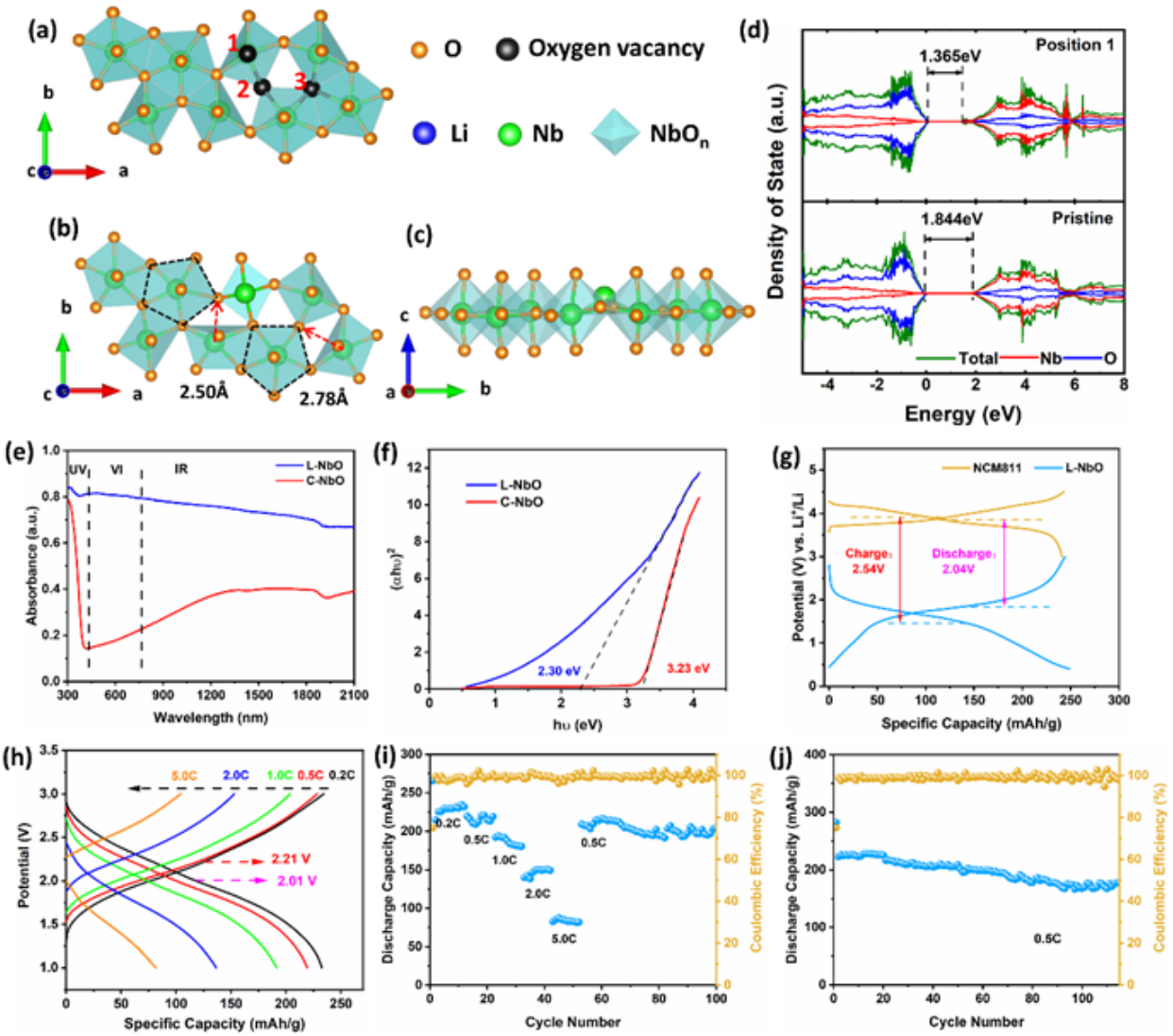

Figure 6. (a) Positions of proposed three different oxygen vacancies in T-Nb_2O_5 from the view of [001] direction. Stable structure of T-Nb_2O_{5-x} with vacancy at Position 1 from the views of (b) [001] and (c) [100] directions. (d) Partial density of states of T-Nb_2O_{5-x} with oxygen vacancies at Position 1 and pristine T-Nb_2O_5. (e) Adsorption spectra and (f) corresponding Tauc plots of L-NbO and C-NbO. (g) Typical charge/discharge curves of L-NbO (at 200 mA/g) and NCM811 (at 140 mAh/g). (h) Charge/discharge curves of L-NbO/NCM811 full cell at different rates based on cathode. (i) Rate performance of L-NbO/NCM811 full cell from 0.2 to 5.0 C. (j) Cycling performance of L-NbO/NCM811 full cell at 0.5C.

TOC

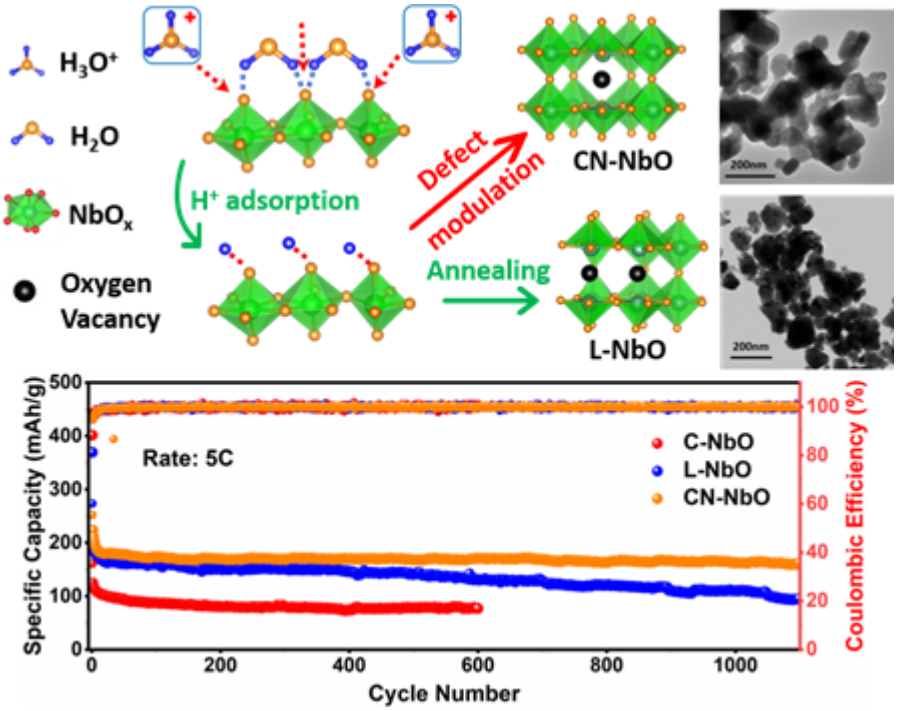

Short summary:

Oxygen vacancies are implanted into T-Nb_2O_5 particles via acid immersion of $Nb_2O_5 \cdot nH_2O$ with the formation of Lewis acid sites. The enrichment of oxygen vacancies endows T-Nb_2O_{5-x} with much higher electric conductivity, better electrochemical kinetics, larger pseudocapacitive contribution. O-doped g-C_3N_4 is creatively proposed as trace oxygen pump to repair excessive oxygen vacancies.